

LASER INTERFEROMETER GRAVITATIONAL WAVE OBSERVATORY  
- LIGO -  
CALIFORNIA INSTITUTE OF TECHNOLOGY  
MASSACHUSETTS INSTITUTE OF TECHNOLOGY

Technical Note	LIGO-T2200205-v1	2022/09/14
<b>Developing an In-Air IR Test Facility for Next-Generation Wavefront Control</b>		
Cassidy Nicks		

**California Institute of Technology**  
**LIGO Project, MS 18-34**  
**Pasadena, CA 91125**  
Phone (626) 395-2129  
Fax (626) 304-9834  
E-mail: info@ligo.caltech.edu

**Massachusetts Institute of Technology**  
**LIGO Project, Room NW22-295**  
**Cambridge, MA 02139**  
Phone (617) 253-4824  
Fax (617) 253-7014  
E-mail: info@ligo.mit.edu

**LIGO Hanford Observatory**  
**Route 10, Mile Marker 2**  
**Richland, WA 99352**  
Phone (509) 372-8106  
Fax (509) 372-8137  
E-mail: info@ligo.caltech.edu

**LIGO Livingston Observatory**  
**19100 LIGO Lane**  
**Livingston, LA 70754**  
Phone (225) 686-3100  
Fax (225) 686-7189  
E-mail: info@ligo.caltech.edu

## 1 Abstract

Thermally-induced defects, particularly point absorbers, are a persistent problem in ramping up LIGO’s power to lower the quantum noise floor (the sensing limit imposed by photon shot noise). One proposed solution is to use a ring heater adaptive optics device to project a thermal correction map onto the LIGO test masses to minimize the scattering into higher order modes. In order to test this concept, an in-air infrared (IR) test facility, with a focus on the control of the IR camera, is developed. Using an IR-absorptive thin screen with an IR camera behind it, the thermal maps created by the ring heater can be tested and refined. By developing code to control the camera, particularly fine-tuning control over temperature measurements, these thermal maps and their effectiveness can be accurately analyzed.

## 2 Introduction

In 1893, gravitational waves were first proposed by Oliver Heaviside when noting the similarities between the inverse square laws of electrical charges and gravity; a little over a decade later, Henri Poincaré proposed that these possible waves would have to move at the speed of light [1, 2]. However, it was not until Einstein’s Theory of General Relativity in 1916 that gravitational waves were predicted by a physical model [3]. In essence, gravitational waves can be described as ripples in spacetime caused by accelerating massive objects. The strongest, and thus most measurable, gravitational waves are caused by huge astronomical events like colliding black holes and neutron stars, as well as supernovae. Unlike electromagnetic radiation, gravitational waves only weakly interact with matter between source and detection, making them invaluable tools for understanding the mechanisms of their sources. After Einstein’s predictions, however, the existence of gravitational waves was hotly debated, even by Einstein himself. It took until 2015 for gravitational waves, caused by two colliding black holes, to be directly detected at aLIGO (advanced Laser Interferometer Gravitational-wave Observatory).

aLIGO’s construction, building on the initial LIGO model, began in 2008. LIGO is essentially a set of two massive Michelson interferometers, one in Louisiana and one in Washington, with 4 km long perpendicular arms that form an L-shape (see Figure 1). In essence, lasers are sent through the arms, reflected off mirrors at their ends, and then recombined at a photodetector between the two arms. As gravitational waves pass, they stretch spacetime in one direction, causing an interference pattern between the lasers in the two arms. This interference pattern can be measured to understand the character of the wave and, by extension, the event that produced it. However, the precision necessary to detect gravitational waves means any noise can be detrimental to results. The work transitioning from LIGO to aLIGO and current work to improve aLIGO has been focused on reducing noise. The greatest source of noise in aLIGO is quantum noise [5]. One way to decrease quantum fluctuations, however, is to increase the power used: photon shot noise decreases as the number of photons increases (by a factor of  $\frac{1}{\sqrt{N}}$ ).

A multitude of additional optics are added to the interferometer to boost the sensitivity of the system. A power recycling cavity, the arm cavities (Fabry Perot cavities), and a signal recycling cavity form four coupled laser cavities within aLIGO for this purpose (Figure 2).

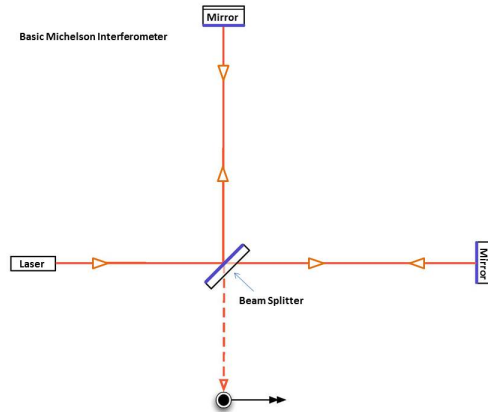


Figure 1: Basic diagram, from the LIGO website showing the Michelson interferometer setup that is the basis of the design of LIGO [4].

Power recycling mirrors form the first cavity, which allows laser light that has been sent through the system to be reflected back through it, thus “recycling” the laser power. The arm cavities are Fabry Perot cavities, which bounce incoming laser light between two mirrors about 300 times, increasing the distance the light travels and building up the laser light in the system. Finally, the signal recycling mirror forms an anti-resonant optical cavity that extracts only the frequency of light associated with a signal, thus allowing it to be “tuned” to see specific gravitational wave signals.

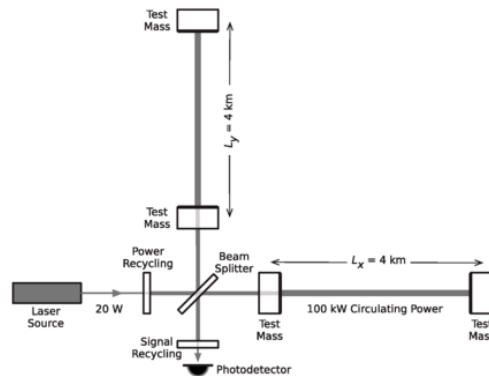


Figure 2: Simplified LIGO diagram showing the Michelson interferometer setup with the power recycling, Fabry Perot, and signal recycling cavities. Modified from Figure 3 in [6].

While these additional optics are imperative to creating a system with enough sensitivity to detect gravitational waves, increasing the power can introduce or amplify other sources of noise or optical losses. In particular, thermal noise, such as through the deformation of the test mass substrate as the coating absorbs power, is amplified. The current system to address this is the Thermal Compensation System (TCS). The TCS adaptive optic system that addresses uniform coating absorption within the Fabry Perot cavities is current ring heater actuators. These ring heaters apply a quadratic correction, working towards zero residual power of surface deformation, to the deformed test mass substrate by adjusting its

radius of curvature [7]. This correction is inversely-related to the test mass deformation near the center, but is mismatched at the edges of the test mass. In general this mismatch is negligible as the fundamental Gaussian mode of the laser, which LIGO is sensitive to, only hits the center of the test mass. However, as the power of the laser increases, so does the deformation. Eventually this mismatch between the deformation produced by the mirror’s self heating and the deformation purposefully driven by the ring heater becomes limiting as the deformed edges of the correction infringe on the area that the fundamental laser mode strikes.

Another source of thermal noise that the TCS is unable to address is nonuniform thermal effects. One such example is from defects that are physically present in mirrors from their fabrication, particularly point absorber defects [5]. These point absorber defects arise as small defects (mainly aluminum flecks) from fabrication heat up and become nearly 100% absorptive, scattering laser light out of the fundamental mode and into higher order modes. When laser light is scattered into these higher order modes, there is less power in the fundamental mode and the sensitivity of aLIGO is adversely affected. Effects like this cause the actual arm power to fail to reach the design power of aLIGO, as seen in Figure 3.

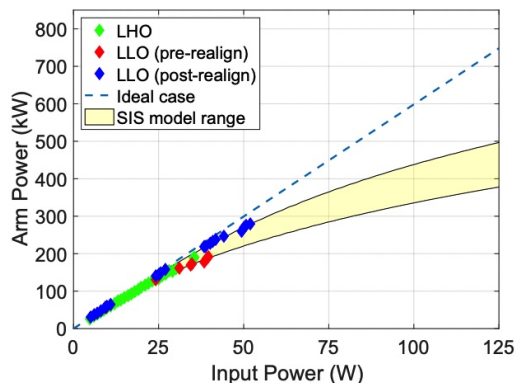


Figure 3: aLIGO ideal vs. actual arm power vs. input power circa O3. Figure from Brooks et al. 2021, P1900287.

One proposed solution to the limitations noted here is a next generation ring heater actuator designed to address higher order modes (HOM ring heater) [8]. While the Richardson lab has extensive theoretical models of this HOM ring heater, there is still need to experimentally test that the HOM ring heater will perform as expected, hopefully in time for the O4 run. Our project for the summer of 2022 was to create an in-air facility with a setup to test the HOM ring heater and other future adaptive optics that counteract these and, ideally, other thermally-induced mirror deformations in aLIGO. The key components of the facility include an infrared-detecting camera, a thin screen to act as a test mass, and the annular ring heater developed by Dr. Richardson and his colleagues [8].

### 3 Objectives

In order to produce extremely low loss laser cavities, this project sought to:

1. Construct an in-air optical test facility to allow for the testing of infrared adaptive optics systems.
2. Develop Python code to collect raw data from the infrared sensor in order to test current and future wavefront controlling technology.

## 4 Methods

### 4.1 Optical System Setup

The first two weeks of this project were dedicated to setting up the in-air optical table system using a simple triangular optical setup with the ring heater, the IR-absorbing thin screen, and the infrared camera, as in Figure 4. The ring heater, which will have an inner diameter of 0.34 m in its final iteration, will allow for manipulation of the radiation that hits the 0.4 x 0.5 m IR absorbing screen (in place of the 0.34 m test mass in the aLIGO system). The screen, which is 0.1mm thick, is thin enough that the infrared-sensitive camera will be able to detect and map the effects of the ring heater on the test mass based on the image of the back of the screen (the width of the screen is negligible to understanding the infrared pattern).

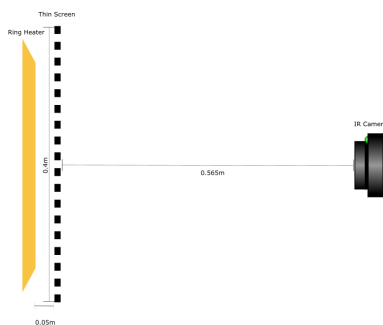


Figure 4: Optical diagram of the in-air IR test facility setup.

One key component of this system is the infrared camera. The IR camera uses microbolometers to detect infrared radiation based on changing electrical resistance, which the camera records as raw ADC values [10]. The microbolometers are arranged in a 640 x 480 array in the camera used for this iteration of the in-air test facility (the Teledyne FLIR A70). Notably, the camera also has a visual camera with a resolution of 1280 x 960 pixels and is used for specific camera modes; however, it is the field of view of the IR camera that is limiting. The IR camera has a 51° x 39° field of view. In order to allow the camera to capture stray

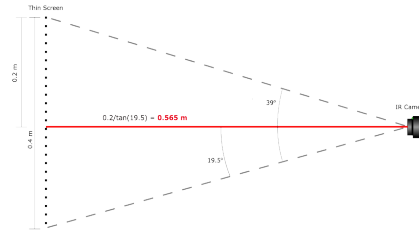


Figure 5: FOV calculation to determine camera distance from screen.

light bouncing off the test mass, 0.4 m, the height of the thin screen, is defined as the desired diameter of the camera's view. Using the vFOV,  $39^\circ$ , the equation  $l = \frac{0.4}{2}\tan(\frac{39^\circ}{2})$  yields a distance of 0.565 m. Thus, the camera must be 0.565 m from the screen to contain the entire 0.4m area in its FOV while still maximizing the FOV (as in Figure 5).

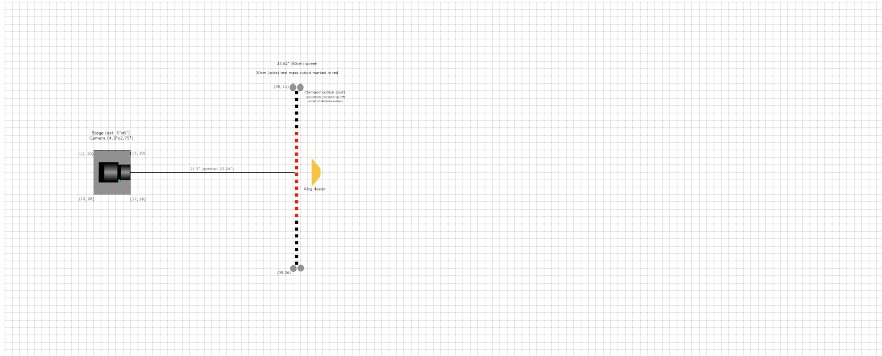


Figure 6: Optical diagram of the in-air IR test facility setup based on the table dimensions (1" x 1" grid).

Once the correct distances were determined, the table was set up. The table is 4'x10' and the desired optical layout was concentrated on the left side of the table, as in Figure 6. This allows for the most effective use of space and for easier fine adjustment of the camera. The heater system shown in Figures 6 and 7 is a smaller version for proof of concept of the ring heater shown in Figure 4. The IR-absorbing screen was mounted first and has the outline of a test mass painted onto it, allowing the pattern from the heater system and, eventually, the ring heater to be analyzed within the parameters of its use in LIGO. This set up, pictured in 7, is meant to allow for end-to-end validation of the experimental setup [9]. Once the setup has been validated with the heater system and the HOM ring heater prototype is available, the heater system will be swapped out for the prototype. However, the rest of the system should already be optimized and not need any major adjustments.

The camera is mounted on a combination of stages that allows for x, y, z, and rotational fine-tuning. The camera was finely adjusted so that the screen just barely filled the FOV, as predicted in the FOV measurements, by slowly adjusting each degree of freedom.

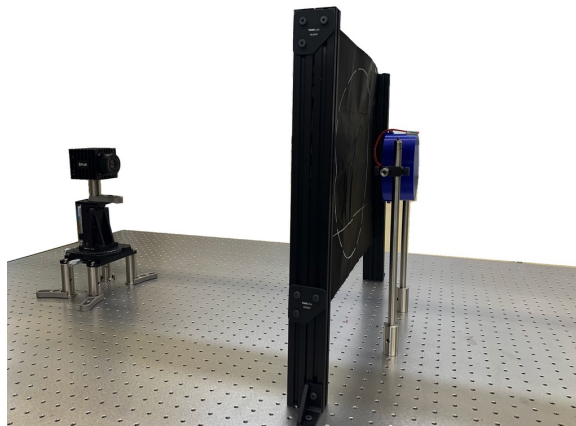


Figure 7: Image of the optical table setup. From left to right: IR camera, IR-absorptive screen, heater system standing in for HOM ring heater prototype.

## 4.2 Controlling the IR Camera

The second portion of this project was to create Python code in order to collect data from the IR camera. In particular, the ability to measure temperature enables us to collect experimental data for comparison with our theoretical models. Building on the existing API, this code allows for the camera settings to be configured, then collects and displays data characterizing the pattern added to the thin screen by the ring heater.

The interface created allows for snapshots of the screen to be taken and for a stream of snapshots to be displayed as live imaging from the camera. When configured to the appropriate settings, which are user inputted values set via a YAML configuration file, the images include a color bar that characterizes the temperature of the image, as in Figure 8. Multiple imaging modes are available, including visual, thermal, and various filtered modes.

This code will be used for all upcoming work with this camera with the end goal of using the camera to determine the best heating pattern from the HOM ring heater in order to mitigate power loss from the point sources in aLIGO's mirrors.

### 4.2.1 Calculating Temperature

Converting intensity measurements to temperature is a nonlinear, complex process with limited accuracy. However, the FLIR A70 camera has an associated calibration curve that guarantees an error of  $\pm 2\%$  within our desired temperature range when object parameters are correctly defined [11]. There are eight object parameters: reflected temperature, atmospheric temperature, object distance, object emissivity, relative humidity, external optics temperature, external optics transmission, and estimated transmission. These parameters

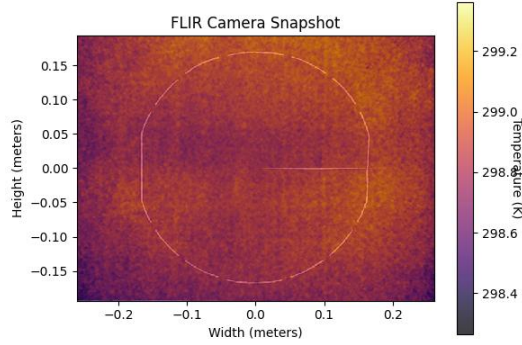


Figure 8: Python interface when measuring temperature.

work to account for both the radiance of the object being observed, as well as radiation from the atmosphere and radiation from nearby objects that reflects off the object of interest, as in equation 1. Equation 1 calculates the total incident radiation power based on the radiation power from these three instances. These incident radiation values are acted on by  $\epsilon$ , the emissivity, and  $\tau$ , the transmission, as expected by the total radiation law (see Appendix A).

$$W_{tot} = \epsilon\tau W_{obj} + (1 - \epsilon)\tau W_{refl} + (1 - \tau)W_{atm} \quad (1)$$

We can assume the incident radiation power is proportional to the camera signal. Thus, we find the object itself induces some camera signal that is only part of the total camera signal, as in Equation 2. The various camera signals can be determined by the object parameters. The process is somewhat lengthy, but a full description is included in Appendix B.

$$U_{obj} = \frac{1}{\epsilon\tau}U_{tot} - \frac{1 - \epsilon}{\epsilon}U_{refl} - \frac{1 - \tau}{\epsilon\tau}U_{atm} \quad (2)$$

To go from this raw input signal to temperature requires two major steps dependent on camera parameters that FLIR automatically determines for each camera during their calibration process: offset ( $J_0$ ), gain ( $J_1$ ), R, B, and F. First, to convert this signal into a raw 16 bit signal, as demanded by the Mono16 pixel format the camera uses, the offset ( $J_0$ ) is added to the signal, then the sum is multiplied by the gain ( $J_1$ ). The offset accounts for the internal temperature of the camera, while the gain accounts for the automatic gain applied by the camera meant to ensure the camera signals measured fill the full 16 bit value range. This is set equal to what is known as the RBF function, which is an approximation of Planck's Law commonly used for thermal imaging [12].<sup>1</sup> The result is equation 3.

$$(U_{obj} + J_0)J_1 = \frac{R}{e^{\frac{B}{T}} - F} \quad (3)$$

<sup>1</sup>For Planck's Law, see Appendix A.



This equation can be solved for temperature, yielding equation 4. Notably, the only unknown in this equation is the input signal,  $U_{obj}$ , for which we have an expression from equation 2.

$$T = \frac{B}{\ln\left(\frac{R}{(U_{obj} + J_0)J_1} + F\right)} \quad (4)$$

These expressions were incorporated into the code for the thermal camera image to yield temperature values based on the intensity that the camera measured.<sup>2</sup>

#### 4.2.2 Error Analysis

In order to express our confidence in the temperature measured by the camera, an analysis of calibration error is necessary. The method for calculating temperature mentioned in the previous section depends on multiple input parameters, as outlined in Appendix A. Each of these input parameters has a certain amount of estimated error. Given the number of free parameters, the chosen method for evaluating calibration error was through a Monte Carlo simulation.

A Monte Carlo simulation allows us to simulate a distribution of realistic measurements for temperature based on one raw value input. First, we define a distribution of values, based on the uncertainty, for each parameter (see Appendix C). We defined each parameter as the value it holds within the lab in a cold state and created a random normal distribution for it. Choosing a random value within these distributions for each parameter, we can calculate a temperature that contains some uncertainty related to the expected, theoretical temperature. By doing this for multiple trials and normalizing by the expected temperature, we obtain a distribution whose standard deviation represents the uncertainty of a temperature measurement for that specific input signal. Figure 9 shows a histogram of the distribution for the raw ADC value 25000.

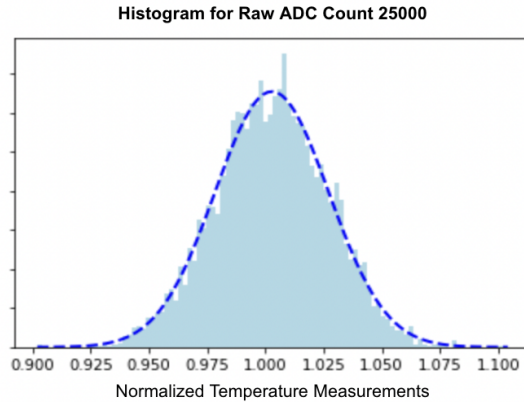


Figure 9: Example of histogram used to determine error in a Monte Carlo simulation for the input signal 25000.

<sup>2</sup>The code was largely provided by FLIR’s measurement formula [13].

Calibration error will also vary based on the input raw value. By running the simulation for a range of possible values, this relationship can be seen. It mimics the RBF function, which is as expected. Figure 10 shows the simulated data and fit lines for this distribution. The inverse natural log curve fit, close to the RBF function, is shown and fits well. However, the seventh degree polynomial has more degrees of freedom that allows it to better represent that data. The  $\chi^2$  value is less than  $\frac{1}{5}$  for the polynomial fit line as compared to the inverse natural log fit. The polynomial with determined coefficients continued to fit the data well even after running this fit simulation multiple times, implying the fit was good, rather than just conforming to current data. This polynomial was incorporated into the snapshot function of the camera streaming GUI, exporting a CSV file with the location, temperature, and uncertainty for each pixel within the snapped image.

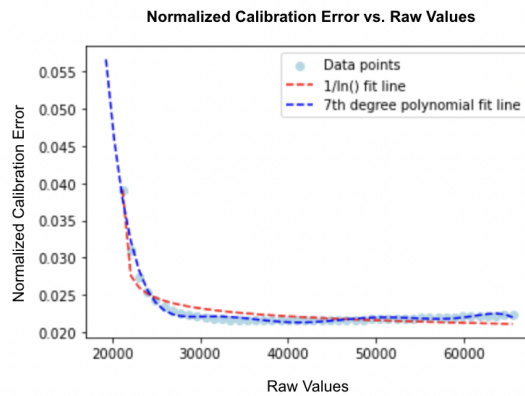


Figure 10: Plot of normalized error vs. input signal with fit lines.

### 4.2.3 Combining Visual and Thermal Information

One of the main goals of this software was to simultaneously display temperature values and a combination of both visual and thermal images, as exemplified by FLIR's Multi-Spectral Dynamic Imaging, or MSX. MSX overlays details from the visual camera on top of the thermal image from the IR camera to help define the IR image. Unfortunately, the temperature equation identified above (equation 4) is only valid when the camera is acquiring images in the Mono16 pixel format, while MSX only works in the Mono8 pixel format.

To incorporate visual image details into the display, the chosen compromise was to overlay a static visual image of the system on the thermal information. Because the camera is stable and locked in place, the visual image should remain static and thus overlaying a singular visual image is acceptable. The accuracy of this can be crosschecked by using the overlay in conjunction with the MSX imaging mode and crosschecking their alignment. In the case of the system being changed or knocked askew, acquiring a new image is a simple process represented within the main interface's code.

#### 4.2.4 Final Interface

The final interface created for this project is a Matplotlib window displayed via PyQT5 that performs all of the functions mentioned in Section 4 (see Figure 11). Using a variety of buttons, the live stream of images can be saved as a snapshot at a particular instance with the inherent data exported, alongside the error. The temperature displayed is based on the minimum and maximum values within the camera’s field of view, which can be re-determined via the use of another button. A separate button acquires a new visual overlay image, which can be toggled on and off.

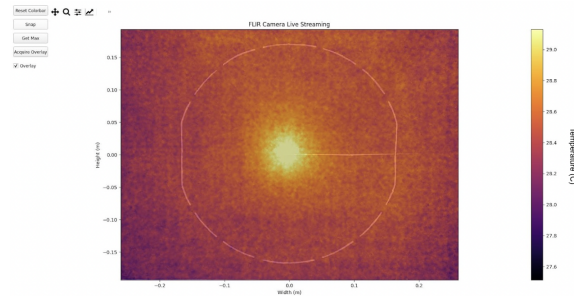


Figure 11: Final Matplotlib interface enabling live camera streaming functionality.

## 5 Summary and Next Steps

Currently, the system has a functioning IR camera with code for streaming and taking snapshots, as well as determining error for each measurement. The end-to-end validation of the system was completed by Phoebe Zyla and Ryan Andersen [9]. The in-air optical test facility is ready to be used to test the prototype HOM ring heater. This new ring heater seeks to address many of the limitations of the current TCS and future iterations will have even more applications, facilitating the lowering of aLIGO’s quantum noise floor and increasing the sensitivity of the instrument.

## 6 Acknowledgements

Thank you to my mentor, Tyler Rosauer, and Dr. Richardson, as well as the other mentors and students for their support and knowledge throughout this project. I would also like to acknowledge the NSF, UC Riverside and the Caltech SURF program, as well as LIGO Laboratory, for giving me this wonderful opportunity.

## References

- [1] Heaviside, Oliver, *A Gravitational and Electromagnetic Analogy*. The Electrician, (1893).

- [2] Poincaré, Henri, *Sur la dynamique d' l'électron*. Comptes Rendus of the French Academy of Sciences 140, 1504-1508 (1905).
- [3] Einstein, Albert, *Integration Neherungsweise Feldgleichungen der der Gravitation*. Sitzung der phsikalisch-mathematischen Klasse, 688-696 (1916).
- [4] <https://www.ligo.caltech.edu/page/ligos-ifo>
- [5] Brooks, A. F., Vajente, G., Yamamoto, H., Abbott, R., Adams, C., Adhikari, R. X., Ananyeva, A., Appert, S., Arai, K., Areeda, J. S., Asali, Y., Aston, S.M., Austin, C., Baer, A. M., Ball, M., Ballmer, S. W., Banagiri, S., Barker, D., Barsotti, L., ... Zweizig, J., *Point Absorbers in Advanced LIGO*. Applied Optics 13, (2021).
- [6] Abbott, B. P., Abbott, R., Abbott, T. D., Abernathy, M. R., Acernese, F., Ackley, K., Adams, C., Adams, T., Addesso, P., Adhikari, R. X., Adya, V. B., Affeldt, C., Agathos, M., Agatsuma, K., Aggarwal, N., Aguiar, O. D., Aiello, L., Ain, A., Ajith, P., ... Zweizig, J., *Observation of Gravitational Waves from a Binary Black Hole merger*. Physical Review Letters 116 (2016).
- [7] Brooks, A. F., Abbott, B., Arain, M. A., Ciani, G., Cole, A., Grabeel, G., Gustafson, E., Guido, C., Heintze, M., Heptonstall, A., Jacobson, M., Kim, W., King, E., Lynch, A., O'Connor, S., Ottaway, D., Mailand, K., Mueller, G., Munch, J., ... Willems, P., *Overview of Advanced LIGO Adaptive Optics*. The Optical Society 55, (2016).
- [8] Richardson, Jonathan, *Active Wavefront Control for Megawatt Arm Power*. LVK Meeting, (2022).
- [9] Zyla, P., Andersen, R., Richardson, J., *A Calibrated Blackbody Source for Testing Next-Generation Wavefront Actuators*. LIGO-T2200206-v6, (2022).
- [10] [https://www.flir.com/products/a50\\_a70-research-amp-development-kits/?model=89951-0201&vertical=research-and-development-science&segment=solutions](https://www.flir.com/products/a50_a70-research-amp-development-kits/?model=89951-0201&vertical=research-and-development-science&segment=solutions)
- [11] Teledyne FLIR, *FLIR A50/A70 Datasheet*. (2022).
- [12] Sundin, Petter, *Intuitive Colorization of Temperature in Thermal Cameras*. 72, (2015).
- [13] [https://flir.custhelp.com/app/answers/detail/a\\_id/3321/related/1](https://flir.custhelp.com/app/answers/detail/a_id/3321/related/1)

## 7 Appendix A: Useful Equations

The total radiation law used to determine the coefficients in equation 1, where  $\alpha$  refers to incident energy absorption,  $\rho$  to reflection, and  $\tau$  to transmission:

$$W = \alpha W + \rho W + \tau W \quad (5)$$

Planck's Law, from which the RBF function (3) is derived ( $\nu$  is the electromagnetic radiation frequency):

$$B(\nu, T) = \frac{2h\nu^3}{c^2} \frac{1}{e^{\frac{hc}{k_B T}} - 1} \quad (6)$$

## 8 Appendix B: Object Parameters

Reflected Energy Parameters:

- Object Emissivity: Based on only the IR-absorptive screen, which has an emissivity of 0.9999 according to manufacturer's specifications.
- Object Distance: Calculated based on final placement of aligned camera. In our case, 0.546m.
- Reflected Temperature: In our case assumed to be the same as the atmospheric temperature, 295K.

Atmospheric Attenuation Parameters:

- Atmospheric Temperature: Determined based on the room conditions. In our case, assumed to be 295K.
- Relative Humidity: Determined based on room conditions. In our case, assumed to be 0.5.
- Estimated Transmission: In our case, assumed to be 1.0.

External Optics Parameters:

- External Optics Temperature: In our case, assumed to be 293.15K.
- External Optics Transmission: In our case, assumed to be 1.0.

We recall from equation 2 that in order to determine the radiance resulting from the object's temperature alone ( $U_{obj}$ , we need to determine  $U_{tot}$ ,  $U_{amb}$ , and  $U_{atm}$ .

$U_{tot}$  is simply the data collected by the camera. The transmission from equation 2 ( $\tau$ ) includes both the transmission from the reflected environment and from the external optics in use. FLIR refers to the measured radiance from the reflected environment, atmosphere and external optics as "pseudo radiance" from the object.

$U_{amb}$  refers to the ambient objects' radiance, which reflects off of the imaged object. This depends on emissivity of the object and the reflected temperature parameter. Using these values, the RBF function (equation 3) can be applied to determine the theoretical signal from the reflected environment.

$U_{atm}$  includes the pseudo-radiance of the atmosphere and the pseudo radiance of the external optics, as both rely on the same coefficients. However, the transmission factors ( $\tau$ ) are

different in each case, hence there being a separate object parameter for the external optics transmission. As for  $U_{amb}$ , these values are calculated using the RBF function (equation 3) to determine the expected signal of the pseudo radiance of the atmosphere and the external optics.

## 9 Appendix C: Free Parameter Uncertainty

Input parameter uncertainty was defined by the specificity of each measurement (except the camera calibration parameters, which had defined uncertainty from the manufacturer).

Camera Calibration Parameters Estimated Uncertainty (2% of the camera-defined value):

- R:  $R*0.02$
- B:  $B*0.02$
- F:  $F*0.02$
- $J_0$ :  $J_0*0.02$
- $J_1$ :  $J_1*0.02$

Reflected Energy Parameters Estimated Uncertainty:

- Object Emissivity: 0.0001
- Object Distance: 0.01
- Reflected Temperature: 0.01

Atmospheric Attenuation Parameters Estimated Uncertainty:

- Atmospheric Temperature: 0.01
- Relative Humidity: 0.1
- Estimated Transmission: 0.001

External Optics Parameters Estimated Uncertainty:

- External Optics Temperature: 0.01
- External Optics Transmission: 0.001